

# Neural-Network-Based Source Reconstruction for Estimating Linear Synchronous Motor Radiation

Lu Xing<sup>1, 2</sup>, Yinghong Wen<sup>1, 2, 3</sup>, David W. P. Thomas<sup>4</sup>,  
Jinbao Zhang<sup>1, 2</sup>, and Dan Zhang<sup>1, 2, \*</sup>

**Abstract**—An equivalent source model based on neural network is proposed to rapidly estimate the magnetic radiation characteristics of linear synchronous motor (LSM) in electromagnetic suspension (EMS) maglev system. The equivalent source is composed of electric dipoles and a closed three-dimensional (3-D) surface, and is developed in terms of source reconstruction method. A few sampling data of magnetic field simulation results serve as the input information to determine the unknown current distribution on equivalent source model. To solve the inverse radiation problem and characterize the whole radiation pattern with high efficiency, the current distribution signature of equivalent model is fitted into artificial neural network models. Separate neural network models are fitted under different phases of winding excitation, which enables the low-frequency magnetic field estimation under both 3-phase balanced operation and unbalanced operation. The equivalent source model is extended to estimate LSM radiation in multi-source environment, and the comparison with numerical simulation verifies its accuracy and efficiency.

## 1. INTRODUCTION

Long stator linear synchronous motor is the driving force supply and electrical power supply for high-speed EMS maglev train [1–4]. When the three-phase windings embedded in LSM stator are powered up by high driving current, LSM establishes an electromagnetic (EM) field and renders itself a major radiation emission source in maglev system [5]. As LSM operates at a frequency range under 400 Hz, its low-frequency magnetic radiation attracts more attention among researchers. It is reported in [6] that the radiated low-frequency magnetic field of LSM would interfere with sensing devices mounted under train body. [7] and [8] evaluate the electromagnetic environment of maglev system with various operating conditions of LSM, which indicate that the magnetic radiation of LSM with short-phase fault is nearly 10 times larger than that under normal operating condition. Similar to maglev system, other vehicular systems driven by three-phase motor are facing the similar electromagnetic compatibility (EMC) problem. [9] and [10] both mention cases on motor radiation emission interference with the normal operation of on-board signal receivers and electronic devices. Meanwhile, as a symbol of enhancing public health awareness, biomedical effects of low-frequency magnetic exposure caused by electrical devices become an subject of intense scholarly discussion [11–16]. Unlike traditional motor devices, LSM stator installed along maglev route is not enclosed in metal shell or train body during operating, which makes surrounding equipment and living organisms directly exposed to its radiation field. As a result, the evaluation of LSM radiation should be carefully considered both for sensitive equipment protection and human healthcare at maglev vehicle design stage.

---

*Received 12 July 2021, Accepted 13 September 2021, Scheduled 26 September 2021*

\* Corresponding author: Dan Zhang (zhang.dan@bjtu.edu.cn).

<sup>1</sup> Beijing Engineering Research Center of EMC and GNSS Technology for Rail Transportation, Beijing 100044, China. <sup>2</sup> Institute of Electromagnetic Compatibility, Beijing Jiaotong University, Beijing 100044, China. <sup>3</sup> Frontiers Science Center for Smart High-speed Railway System, Beijing 100044, China. <sup>4</sup> George Green Institute for Electromagnetics Research, University of Nottingham, Nottingham, UK.

However, due to the lack of effective analysis method, researches on radiation emission of motor devices and motor drive systems are relatively few [17]. As the standard experimental procedures to assess motor radiation characteristics are expensive and maintenance-extensive [18], it is not practical to adopt measurement method in estimating motor radiation at EMC design stage. Another common method to estimate motor radiation is using electromagnetic field numerical calculation method [9, 19]. Numerical method is capable to calculate the radiated characteristics of motor devices with any operating condition in any environment. However when multi-source environment and large-scale computational region are involved, the motor's complex structure causes a long computation time and large memory footprint to numerical computation process [20]. Hence, some researchers make attempts to simplify motor structure using source reconstruction method and to further reduce the complexity of EM computation.

Source reconstruction method is widely used in antenna diagnosis and near-field-to-far-field (NF-FF) transformation [21, 22], and further applied in realms of EMC to predict the radiation field at arbitrary distance from the radiating source [23–25]. The underlying idea of source reconstruction method is to replicate the radiation characteristics of a complex radiating system with a simplified model composed of a set of equivalent sources. The current distribution of equivalent source can be determined by solving the Inverse Radiation Problem (IRP) with the observed near-field characteristics of original source as a known factor. Hence the equivalent source could be constructed, and the far-field radiation could be estimated. Inspired by its high precision in reproducing complete electromagnetic characteristics, this method is applied to the equivalent source modelling of electrical and electronic devices in a number of papers [26–30]. However, numerically, the IRP can be formulated as a system of linear integral equations. The solving process of the complex linear system is always a challenge in practice. To overcome these drawbacks, a number of optimization based techniques to reduce the computational cost of IRP are developed [31]. In [32], a simplified wire model is developed in simulation software for reproducing the far-field electromagnetic radiation of an actual motor machine. Serving the observed magnetic field of detailed geometric models as the input information of IRP, the unknown current on each wire of simplified wire model is solved by Particle Swarm Optimization (PSO). However, the number of the unknown factors in Swarm Intelligence Algorithm is often strictly limited due to the complex searching procedure, which limits the optimal performance of equivalent source model.

In recent years, developments in artificial neural network platform provide us with a more efficient way of data modelling. Several studies on neural network applications prove that a fairly simple artificial neural network could achieve satisfying accuracy in predicting EMC problems. In [33], a dipole is employed to replace motor devices in vehicle models to reduce computation time in motor radiation simulation. The establishment process of this dipole model does not involve any physical principle, and the relationship between the dipole size and excitation and its electric field intensity at a certain observation point is directly established through the neural network. This dipole model is reported to be capable to approximate the motor's radiation characteristics with high efficiency. However, the oversimplified modelling process makes the dipole model lack flexibility in estimating motor radiation neither on arbitrary observing area nor in other operation condition.

The aim of this paper is to implement rapid evaluation of LSM low-frequency magnetic radiated characteristics with various working conditions. Therefore, we make use of a high-efficient neural network platform to propose a neural-network-based source reconstruction method for reproducing LSM radiation. To balance the cost efficiency and accuracy of the equivalent model, the stator windings and stator core are modelled as separate equivalent source components. The separate source components enable motor radiation estimation under three-phase balanced condition as well as short-phase fault condition. To reduce the difficulty of source reconstruction process, we employ neural networks for an efficient and accurate solution to Inverse Radiation Problem. In Section 2, we illustrate our methodology to replicate single-segment-length LSM radiation with equivalent model and present corresponding neural-network-based Inverse Radiation Problem. In Section 3, neural networks are developed and trained to produce an equivalent LSM model. The performance of equivalent LSM model is further evaluated and compared with numerical simulation results. Finally, Section 4 gives our conclusion.

## 2. METHODOLOGY

For the purpose of rapid evaluation of LSM radiation, we propose the neural-network based source reconstruction method by following steps: Firstly, we consider LSM as separate source components and analyze the relationship between each source component and overall radiated EM field of LSM. Then, an equivalent LSM model is developed with part of its electrical parameters undetermined. By presenting the radiated characteristics of LSM using unknown parameters of equivalent model, an Inverse Radiation Problem is drawn. Finally, we employ a small number of numerical simulation results as known factor of IRP and embed neural networks in IRP solution. With the above steps, neural networks containing information of equivalent model electrical parameters could be trained and applied to LSM radiated characteristics prediction. The detailed illustration of each step is as follows.

### 2.1. LSM Radiation Analysis

In practical maglev system, for easy installation and maintenance, LSM core is divided into small segments and installed one by one with a gap of a few centimeters between them. Thus, LSM stator exhibits a repetitive structural characteristic with segment length determined by stator core installation. Hereby, in numerical simulation process, the single repeating unit of LSM is normally employed to evaluate its radiated characteristics with infinite-length by adopting master-slave boundary condition. In this paper, we firstly build our equivalent model with single segment length and further extend it to an infinite-length model. The single-segment-length numerical simulation model and equivalent LSM model are shown in Fig. 1.

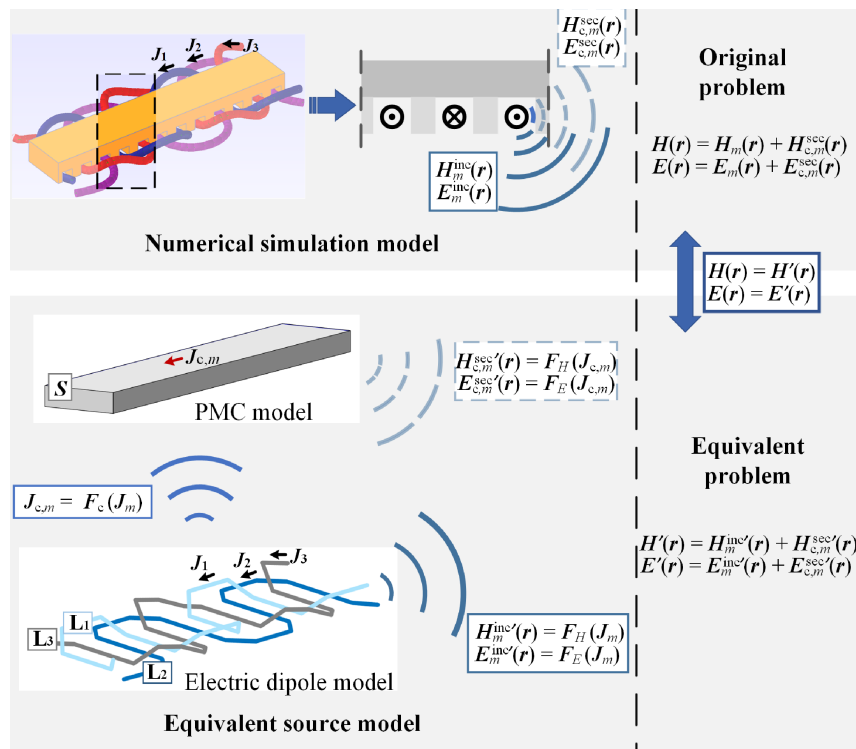


**Figure 1.** Geometric stator model and proposed equivalent source model.

As shown in Fig. 1, the electromagnetic wave generated by stator winding would be incident on stator core and further excite a radiated field. This field could be regarded as a secondary radiation result by reflection, refraction, and diffraction of EM wave on stator core. Therefore, at any given position in free space, the radiated field of LSM stator is formed by the directly incident wave generated

by stator windings and the secondary radiated wave generated by stator core. As the three different phases of motor windings could be treated as three incoherent sources, the radiated characteristics of each winding could be computed separately, and the stator radiated field could be regarded as the superposition of the radiated field excited by each phase of winding. Therefore, at position  $\mathbf{r}$ , the total radiated magnetic field  $\mathbf{H}'$  of stator model could be described as:

$$\mathbf{H}'(\mathbf{r}) = [p_1 \quad p_2 \quad p_3] \begin{bmatrix} \mathbf{H}_1^{\text{inc}' }(\mathbf{r}) + \mathbf{H}_{c,1}^{\text{sec}' }(\mathbf{r}) \\ \mathbf{H}_2^{\text{inc}' }(\mathbf{r}) + \mathbf{H}_{c,2}^{\text{sec}' }(\mathbf{r}) \\ \mathbf{H}_3^{\text{inc}' }(\mathbf{r}) + \mathbf{H}_{c,3}^{\text{sec}' }(\mathbf{r}) \end{bmatrix}. \quad (1)$$

where  $\mathbf{H}_m^{\text{inc}' }$  ( $m = 1, 2, 3$ ) denotes the directly incident magnetic field generated by each winding on  $\mathbf{r}$ , and  $\mathbf{H}_{c,m}^{\text{sec}' }$  ( $m = 1, 2, 3$ ) denotes the secondary radiated field of stator core excited by each winding.  $\mathbf{P} = [p_1, p_2, p_3]$  is a coefficient matrix representing the operating condition of the motor.  $p_m$  ( $m = 1, 2, 3$ ) is set to 1 when the corresponding winding is normally excited while it is set to 0 when the winding is default. By introducing coefficient matrix  $\mathbf{P}$ , it is possible to analyze LSM radiation under normal operating condition ( $p_1 = p_2 = p_3 = 1$ ) as well as short-phase fault condition ( $p_1$  or  $p_2$  or  $p_3 = 0$ ).

## 2.2. IRP in Equivalent Source Modelling

In this paper, we treat the stator core as a radiation source whose radiated characteristics are directly related to the winding radiation. Therefore, the stator windings and stator core are reconstructed as different components with quantitative relationship. As shown in Fig. 1, we regard the curved stator windings as three poly-lines formed by short electric dipoles, which is  $L_m$  ( $m = 1, 2, 3$ ) corresponding to each phase of winding. For the dipoles along each poly-lines, the current value  $\mathbf{J}_m$  ( $m = 1, 2, 3$ ) is equal to the actual current on corresponding stator winging. Define  $\mathbf{r}'_m$  ( $m = 1, 2, 3$ ) as the position vector of points on stator windings,  $L'_m$  ( $m = 1, 2, 3$ ) as the unobscured part of  $L_m$  ( $m = 1, 2, 3$ ) by stator core to  $\mathbf{r}$ . Then it is straightforward to formulate the integral relationship between the winding current  $\mathbf{J}_m$  ( $m = 1, 2, 3$ ) and the magnetic field  $\mathbf{H}_m^{\text{inc}' }$  ( $m = 1, 2, 3$ ) corresponding to each winding source:

$$\mathbf{H}_m^{\text{inc}' }(\mathbf{r}) = \nabla \times \int_{L'_m} \mathbf{J}_m(\mathbf{r}_m) g(\mathbf{r}, \mathbf{r}_m) d\mathbf{r}_m \quad m = 1, 2, 3. \quad (2)$$

where  $g(\mathbf{r}, \mathbf{r}_m)$  ( $m = 1, 2, 3$ ) is the free-space Green's function and is defined as:

$$g(\mathbf{r}, \mathbf{r}_m) = \frac{1}{4\pi |\mathbf{r} - \mathbf{r}_m|} e^{jk|\mathbf{r} - \mathbf{r}_m|} \quad m = 1, 2, 3. \quad (3)$$

The actual stator is complex in terms of geometry. As shown in Fig. 1, we design a 3-D surface model  $S$  based on the Source Reconstruction Method to replicate radiated characteristics of stator core. By means of Love's and Schelkunoff's Field Equivalence Principle, it is possible to simplify the reconstruction procedure by considering only one class of equivalent current [34]. An application case of Schelkunoff's Field Equivalence Principle is explained in Fig. 2. Region I ( $z < z_0$ ) envelops the original source at  $z = -\infty$ , and the equivalent currents are distributed on boundary surface  $z = z_0$ . Region I could be filled up with perfect magnetic conductor (PMC) without affecting the electromagnetic fields

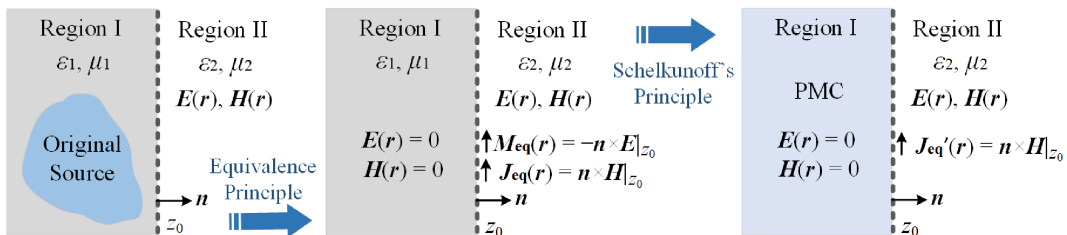


**Figure 2.** Schelkunoff's field equivalence principle.

in both regions, allowing us to take only electric currents into account  $\mathbf{J}'_{\text{eq}}$  over the source domain. Invoke the Image Theory, the field produced by the electric currents  $\mathbf{J}'_{\text{eq}}$  on the region boundary can be obtained, which is twice as much electric equivalent current as in normal case.

In our case, following the Schelkunoff's Field Equivalence Principle, the surface model  $S$  is defined as a cuboid perfect magnetic conductor in a similar size to stator core. As the surface current on cubic surface model is induced by stator windings radiation, we regard the total surface current as the superposition of the induced currents corresponding to each winding. Therefore, assume that the current density on the equivalent core model is  $\mathbf{J}_{c,m}$  ( $m = 1, 2, 3$ ). Then the scattered field  $\mathbf{H}_m^{\text{sec}'}$  ( $m = 1, 2, 3$ ) generated by equivalent core model on  $\mathbf{r}$  could be described as:

$$\mathbf{H}_{c,m}^{\text{sec}'}(\mathbf{r}) = \nabla \times \int_S \mathbf{J}_{c,m}(\mathbf{r}_c)g(\mathbf{r}, \mathbf{r}_c)d\mathbf{r}_c \quad m = 1, 2, 3. \quad (4)$$

where

$$g(\mathbf{r}, \mathbf{r}_c) = \frac{1}{4\pi |\mathbf{r} - \mathbf{r}_c|} e^{jk|\mathbf{r} - \mathbf{r}_c|} \quad m = 1, 2, 3. \quad (5)$$

Then an Inverse Radiation Problem involving the current distribution on  $S$  is formulated. When  $\mathbf{J}_{c,m}$  ( $m = 1, 2, 3$ ) is given, the total magnetic field at  $\mathbf{r}$  could be obtained according to Eqs. (1), (2), and (4).

### 2.3. Neural-Network Based IRP Solution

As the equivalent model attempts to implement the same precision in evaluating LSM radiated characteristics with numerical simulation model, the simulation results could be used as a known factor for IRP. Define  $\mathbf{H}$  as the simulated magnetic field results, then the secondary radiated field  $\mathbf{H}_m^{\text{sec}'}$  ( $m = 1, 2, 3$ ) is:

$$\begin{bmatrix} \nabla \times \int_S \mathbf{J}_{c,1}(\mathbf{r}_c)g(\mathbf{r}, \mathbf{r}_c)d\mathbf{r}_c \\ \nabla \times \int_S \mathbf{J}_{c,2}(\mathbf{r}_c)g(\mathbf{r}, \mathbf{r}_c)d\mathbf{r}_c \\ \nabla \times \int_S \mathbf{J}_{c,3}(\mathbf{r}_c)g(\mathbf{r}, \mathbf{r}_c)d\mathbf{r}_c \end{bmatrix} = \mathbf{P}^{-1} \cdot \mathbf{H}(\mathbf{r}) - \begin{bmatrix} \nabla \times \int_{L'_1} \mathbf{J}_1(\mathbf{r}_1)g(\mathbf{r}, \mathbf{r}_1)d\mathbf{r}_1 \\ \nabla \times \int_{L'_2} \mathbf{J}_2(\mathbf{r}_2)g(\mathbf{r}, \mathbf{r}_2)d\mathbf{r}_2 \\ \nabla \times \int_{L'_3} \mathbf{J}_3(\mathbf{r}_3)g(\mathbf{r}, \mathbf{r}_3)d\mathbf{r}_3 \end{bmatrix}. \quad (6)$$

where

$$\mathbf{H}(\mathbf{r}) = \mathbf{P} \cdot \begin{bmatrix} \mathbf{H}_1(\mathbf{r}) \\ \mathbf{H}_2(\mathbf{r}) \\ \mathbf{H}_3(\mathbf{r}) \end{bmatrix}. \quad (7)$$

and  $\mathbf{H}_m$  ( $m = 1, 2, 3$ ) denotes the simulated magnetic radiation under each phase of excitation. Instead of solving the current density  $\mathbf{J}_{c,m}$  ( $m = 1, 2, 3$ ) specifically, we use an artificial neural network  $\mathbf{net}_m(\cdot)$  ( $m = 1, 2, 3$ ) to map  $\mathbf{J}_{c,m}$  ( $m = 1, 2, 3$ ) and its mathematical relation with the right side of Eq. (6). In order to fit the neural network model of each phase of winding excitation separately, we define  $\mathbf{P}$  as  $[1, 0, 0]$ ,  $[0, 1, 0]$ , and  $[0, 0, 1]$  to obtain 3 sets of training data corresponding to each phase of winding excitation. As shown in Fig. 3, make the Green's function corresponding to a group of observing points as the input matrix of an artificial neural network, and the right side of Eq. (6) corresponding to each observing point as the target output matrix. Then we obtain each phase's IRP solution with neural network model embedded in. With this solution, it is capable to estimate LSM radiation on any observing point or observing face. The radiated magnetic field of stator model on  $\mathbf{r}$  is hereby represented as:

$$\mathbf{H}'(\mathbf{r}) = \mathbf{P} \cdot \begin{bmatrix} \mathbf{H}_1^{\text{inc}'}(\mathbf{r}) + \mathbf{net}_1(\mathbf{r}) \\ \mathbf{H}_2^{\text{inc}'}(\mathbf{r}) + \mathbf{net}_2(\mathbf{r}) \\ \mathbf{H}_3^{\text{inc}'}(\mathbf{r}) + \mathbf{net}_3(\mathbf{r}) \end{bmatrix}. \quad (8)$$

By computing the radiated characteristics on certain observing points with appropriate step size, the full radiation pattern of LSM observing area could be fitted.

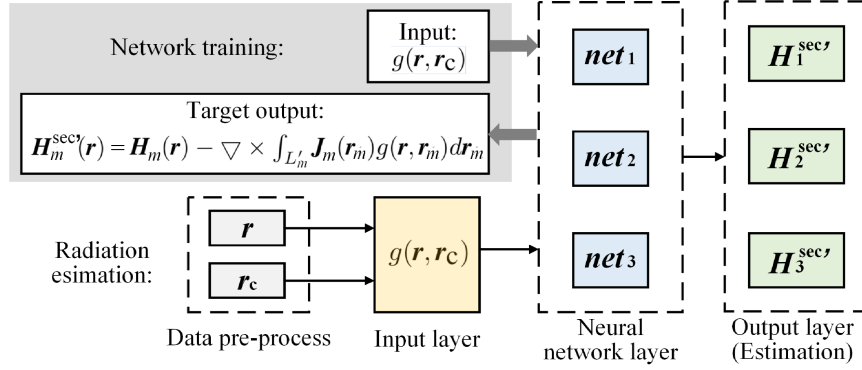


**Figure 3.** The overall structure of source reconstruction based on neural network.

### 3. APPLICATION AND VALIDATION

#### 3.1. Fast Implementation

The modelling procedure discussed in Section 2 presents the neural-network-based source reconstruction method to reproduce the transient radiated electromagnetic field of LSM, and it could be further simplified in application to achieve higher computation efficiency.

The excitation current frequency of LSM is directly related to the running speed of vehicles:

$$v = 2f\tau_p. \quad (9)$$

where  $v$  denotes the vehicle running speed,  $f$  the current frequency of stator winding, and  $\tau_p$  the stator pole pitch. In practical,  $\tau_p = 258$  mm in high-speed maglev. Thus, to power a maglev train with a maximum velocity of 600 km/h, the LSM excitation current frequency is normally in the range of hundreds of Hertz.

When LSM radiation is evaluated within a distance range of tens or even hundreds of meters, the excitation current wavelength  $\lambda$  is sufficiently large compared with the length of stator winding and calculation region. As a result, the phase of the excitation current distributed on stator winding could be regarded as undifferentiated. When the LSM radiation in surrounding area is computed,  $|\mathbf{r} - \mathbf{r}_m|$  and  $|\mathbf{r} - \mathbf{r}_c|$  are minimal in scale compared to wavelength  $\lambda$ , which also indicates that the sinusoidal electromagnetic field excited by LSM has sufficiently low time variations in the computing region. Thus, the radiated electromagnetic field of LSM in the surrounding area could be regarded as a quasi-static field, which means that the transient spatial pattern of LSM radiated magnetic field has the same characteristics as the corresponding magnetostatic field but varies with time [35]. Thus at time  $t$ , the scattered field  $\mathbf{H}_m^{sec}$  ( $m = 1, 2, 3$ ) represented by Eq. (6) could be expressed as:

$$\begin{bmatrix} \nabla \times \int_S \frac{\mathbf{J}_{c,1}(\mathbf{r}_c)}{4\pi|\mathbf{r} - \mathbf{r}_c|} e^{j(\omega t + \varphi_1)} d\mathbf{r}_c \\ \nabla \times \int_S \frac{\mathbf{J}_{c,2}(\mathbf{r}_c)}{4\pi|\mathbf{r} - \mathbf{r}_c|} e^{j(\omega t + \varphi_2)} d\mathbf{r}_c \\ \nabla \times \int_S \frac{\mathbf{J}_{c,3}(\mathbf{r}_c)}{4\pi|\mathbf{r} - \mathbf{r}_c|} e^{j(\omega t + \varphi_3)} d\mathbf{r}_c \end{bmatrix} = \mathbf{P}^{-1} \cdot \mathbf{H}(\mathbf{r}; t) - \begin{bmatrix} \nabla \times \int_{L'_1} \frac{\mathbf{J}_1(\mathbf{r}_1)}{4\pi|\mathbf{r} - \mathbf{r}_1|} e^{j(\omega t + \varphi_1)} d\mathbf{r}_1 \\ \nabla \times \int_{L'_2} \frac{\mathbf{J}_2(\mathbf{r}_2)}{4\pi|\mathbf{r} - \mathbf{r}_2|} e^{j(\omega t + \varphi_2)} d\mathbf{r}_2 \\ \nabla \times \int_{L'_3} \frac{\mathbf{J}_3(\mathbf{r}_3)}{4\pi|\mathbf{r} - \mathbf{r}_3|} e^{j(\omega t + \varphi_3)} d\mathbf{r}_3 \end{bmatrix}. \quad (10)$$

where  $\varphi_1$ ,  $\varphi_2$ , and  $\varphi_3$  are the initial phases of corresponding excitation winding. To further reduce computational complexity, we divide equivalent core model surface into small rectangle meshes. Assume that the mesh quantity is  $N$  and that the current on each rectangle mesh is uniformly distributed. The area and current density under each phase excitation of the  $n$ th mesh are defined as  $\mathbf{S}_n$  and  $\mathbf{J}_{m,n}^c$ . Then

Eq. (10) could be rewritten as:

$$\left[ \begin{array}{l} \sum_{n=1}^N \int_{S_n} \frac{\mathbf{J}_{1,n}^c(\mathbf{r}_c) \times (\mathbf{r} - \mathbf{r}_c)}{4\pi|\mathbf{r} - \mathbf{r}_c|^3} e^{j(\omega t + \varphi_1)} d\mathbf{r}_c \\ \sum_{n=1}^N \int_{S_n} \frac{\mathbf{J}_{2,n}^c(\mathbf{r}_c) \times (\mathbf{r} - \mathbf{r}_c)}{4\pi|\mathbf{r} - \mathbf{r}_c|^3} e^{j(\omega t + \varphi_2)} d\mathbf{r}_c \\ \sum_{n=1}^N \int_{S_n} \frac{\mathbf{J}_{3,n}^c(\mathbf{r}_c) \times (\mathbf{r} - \mathbf{r}_c)}{4\pi|\mathbf{r} - \mathbf{r}_c|^3} e^{j(\omega t + \varphi_3)} d\mathbf{r}_c \end{array} \right] = \mathbf{P}^{-1} \cdot \mathbf{H}(\mathbf{r}; t) - \left[ \begin{array}{l} \nabla \times \int_{L'_1} \frac{\mathbf{J}_1(\mathbf{r}_1)}{4\pi|\mathbf{r} - \mathbf{r}_1|} e^{j(\omega t + \varphi_1)} d\mathbf{r}_1 \\ \nabla \times \int_{L'_2} \frac{\mathbf{J}_2(\mathbf{r}_2)}{4\pi|\mathbf{r} - \mathbf{r}_2|} e^{j(\omega t + \varphi_2)} d\mathbf{r}_2 \\ \nabla \times \int_{L'_3} \frac{\mathbf{J}_3(\mathbf{r}_3)}{4\pi|\mathbf{r} - \mathbf{r}_3|} e^{j(\omega t + \varphi_3)} d\mathbf{r}_3 \end{array} \right]. \quad (11)$$

In practical calculation process, we establish the equivalent model in rectangular coordinate system. Then, for the modelling process under each phase current excitation, it needs to be represented by three vectorial components in the  $x$ ,  $y$ , and  $z$  directions:

$$\begin{aligned} & \sum_{n=1}^N \int_{S_n} \frac{\mathbf{J}_{m,n,y}^c(\mathbf{r}_c) \cdot (r_z - r_{c,z})}{4\pi|\mathbf{r} - \mathbf{r}_c|^3} e^{j(\omega t + \varphi_m)} d\mathbf{r}_{c,x} \\ & = \mathbf{H}_{m,x}(\mathbf{r}; t) - \nabla \times \int_{L'_m} \frac{\mathbf{J}_{m,x}(\mathbf{r}_m)}{4\pi|\mathbf{r} - \mathbf{r}_m|} e^{j(\omega t + \varphi_m)} d\mathbf{r}_{m,x} \\ & \sum_{n=1}^N \int_{S_n} \frac{\mathbf{J}_{m,n,z}^c(\mathbf{r}_c) \cdot (r_x - r_{c,x})}{4\pi|\mathbf{r} - \mathbf{r}_c|^3} e^{j(\omega t + \varphi_m)} d\mathbf{r}_{c,y} \\ & = \mathbf{H}_{m,y}(\mathbf{r}; t) - \nabla \times \int_{L'_m} \frac{\mathbf{J}_{m,y}(\mathbf{r}_m)}{4\pi|\mathbf{r} - \mathbf{r}_m|} e^{j(\omega t + \varphi_m)} d\mathbf{r}_{m,y} \\ & \sum_{n=1}^N \int_{S_n} \frac{\mathbf{J}_{m,n,x}^c(\mathbf{r}_c) \cdot (r_y - r_{c,y})}{4\pi|\mathbf{r} - \mathbf{r}_c|^3} e^{j(\omega t + \varphi_m)} d\mathbf{r}_{c,z} \\ & = \mathbf{H}_{m,z}(\mathbf{r}; t) - \nabla \times \int_{L'_m} \frac{\mathbf{J}_{m,z}(\mathbf{r}_m)}{4\pi|\mathbf{r} - \mathbf{r}_m|} e^{j(\omega t + \varphi_m)} d\mathbf{r}_{m,z} \end{aligned} \quad m = 1, 2, 3. \quad (12)$$

In Eq. (12), the vectors with footprint  $x$ ,  $y$ , and  $z$  denote the vectorial components of a composite vector in corresponding directions. For each single-phase-current excitation condition, define its observing time  $t = (\pi/2 - \varphi_m)/\omega$  ( $m = 1, 2, 3$ ). So that the phase of each current excitation is  $\pi/2$ , and  $e^{j(\omega t + \varphi_m)} = e^{j(0)} = 1$ . Then in Eq. (12), the only unknown quantities are  $\mathbf{J}_{m,n,y}^c$ ,  $\mathbf{J}_{m,n,z}^c$ , and  $\mathbf{J}_{m,n,x}^c$ , which are constant quantities in each corresponding integrating process. Therefore, replacing the known items on left side and right side of Eq. (12) with function  $X$  and  $Y$ , Eq. (12) can be rewritten as:

$$\begin{aligned} & \sum_{n=1}^N \mathbf{J}_{m,n,y}^c(\mathbf{r}_c) \cdot X_{m,n,x}(\mathbf{r}; t)|_{t=(\pi/2-\varphi_m)/\omega} = Y_{m,x}(\mathbf{r}; t)|_{t=(\pi/2-\varphi_m)/\omega} \\ & \sum_{n=1}^N \mathbf{J}_{m,n,z}^c(\mathbf{r}_c) \cdot X_{m,n,y}(\mathbf{r}; t)|_{t=(\pi/2-\varphi_m)/\omega} = Y_{m,y}(\mathbf{r}; t)|_{t=(\pi/2-\varphi_m)/\omega} \quad m = 1, 2, 3. \\ & \sum_{n=1}^N \mathbf{J}_{m,n,x}^c(\mathbf{r}_c) \cdot X_{m,n,z}(\mathbf{r}; t)|_{t=(\pi/2-\varphi_m)/\omega} = Y_{m,z}(\mathbf{r}; t)|_{t=(\pi/2-\varphi_m)/\omega} \end{aligned} \quad (13)$$

In accordance with Eq. (13), for each single-phase-current excitation condition, three neural networks corresponding to three directional components need to be modelled. For instance, by feeding  $X_{1,n,x}(\mathbf{r}; t)|_{t=(\pi/2-\varphi_1)/\omega}$  ( $n = 1, 2, \dots, N$ ) into neural network model as input information, and  $Y_{1,x}(\mathbf{r}; t)|_{t=(\pi/2-\varphi_1)/\omega}$  as target output, the neural network  $\text{net}_{1,x}^{\text{peak}}(\mathbf{r})$  corresponding to the peak value

of the 1st phase sinusoidal-periodic excitation winding could be obtained. Then the total magnetic field on  $\mathbf{r}$  could be reconstructed by the trained neural networks as:

$$\mathbf{H}'(\mathbf{r}; t) = \mathbf{P} \cdot \begin{bmatrix} \left[ \nabla \times \int_{L'_1} \frac{\mathbf{J}_1(\mathbf{r}_1)}{4\pi|\mathbf{r} - \mathbf{r}_1|} d\mathbf{r}_1 + \mathbf{net}_1^{\text{peak}}(\mathbf{r}) \right] e^{j(\omega t + \varphi_1)} \\ \left[ \nabla \times \int_{L'_2} \frac{\mathbf{J}_2(\mathbf{r}_2)}{4\pi|\mathbf{r} - \mathbf{r}_2|} d\mathbf{r}_2 + \mathbf{net}_2^{\text{peak}}(\mathbf{r}) \right] e^{j(\omega t + \varphi_2)} \\ \left[ \nabla \times \int_{L'_3} \frac{\mathbf{J}_3(\mathbf{r}_3)}{4\pi|\mathbf{r} - \mathbf{r}_3|} d\mathbf{r}_3 + \mathbf{net}_3^{\text{peak}}(\mathbf{r}) \right] e^{j(\omega t + \varphi_3)} \end{bmatrix}. \quad (14)$$

where:

$$\mathbf{net}_m^{\text{peak}}(\mathbf{r}) = \text{net}_{m,x}^{\text{peak}}(\mathbf{r}) \cdot \mathbf{i} + \text{net}_{m,y}^{\text{peak}}(\mathbf{r}) \cdot \mathbf{j} + \text{net}_{m,z}^{\text{peak}}(\mathbf{r}) \cdot \mathbf{k}, \quad m = 1, 2, 3. \quad (15)$$

$\mathbf{i}$ ,  $\mathbf{j}$ , and  $\mathbf{k}$  in Eq. (15) denote the unit vectors in  $x$ ,  $y$ , and  $z$  directions, respectively. With the transient magnetic field solution given by Eq. (14), the time-domain low-frequency magnetic field on  $\mathbf{r}$  is presented, and the frequency-domain representation could be decided according to Fourier transformation.

### 3.2. Neural Network Modelling

In this paper, Matlab R2020b is employed to proceed with the computation process and build neural network models. In consideration of the feasibility of network models, we select back propagation neural network (BPNN) to map the surface current signature on stator core. It could be noticed that the input dimension of each neural network model is decided by mesh quantity  $N$  on equivalent core model, while the output dimension is 1. According to the size of equivalent core model, we divide its surface into 52 elements. To obtain training set for BPNN model, a numerical simulation model is built with CST Studio Suite to obtain simulation results. The frequency and amplitude of excitation current of numerical model are defined as 50 Hz and 1 A. The initial phases  $\varphi_m$  ( $m = 1, 2, 3$ ) of each winding are defined as 0,  $2\pi/3$ , and  $4\pi/3$ , respectively. Three separate simulations are carried out to obtain LSM radiation characteristics under each single phase excitation.

As shown in Fig. 4, the observing planes for LSM radiation are located 3 m apart from the top, bottom, and sides of the stator model center. On each observing plane, simulation results are taken as training data with a step size of 0.25 m. Then, for each neural network to be trained, 2400 samples are obtained as the training set (account for 70%), validation set (account for 15%), and testing set (account for 15%).

For a BPNN model, its number of hidden layers is highly related to its ability to express nonlinear problems. Normally, a BPNN with 2 hidden layers is capable to approximate any smooth mapping to any accuracy. Thus, we define the number of hidden layers of BPNN models as 2. The structure of each hidden layer could be decided in accordance with the following empirical formula:

$$N_h = \frac{N_s}{\alpha \cdot (N_i + N_o)}. \quad (16)$$

where  $N_h$  denotes the number of neurons in hidden layers,  $N_s$  the number of samples in training set, and  $N_i$  and  $N_o$  denote the numbers of neurons in input layer and output layer, respectively.  $\alpha$  in Eq. (16) is a customized variable which normally ranges from 2 to 10. In this paper, we define  $\alpha = 4$ ; therefore, the number of hidden layers of each neural network models is decided as 12.

The developed neural networks are trained by Levenberg-Marquardt algorithm, and network training processes are set to stop when generalization stops improving. The performances of trained networks are evaluated using adjusted R-squared  $R_{adj}^2$ . Adjusted R-squared  $R_{adj}^2$  is the degree-of-freedom adjusted coefficient of determination, which describes the proportionate amount of variation in the response variables explained by the independent variables in the multiple linear regression.  $R_{adj}^2$  is defined as:

$$R_{adj}^2 = 1 - \frac{\text{SSE}}{\text{TSS}} \frac{a - 1}{a - b - 1}. \quad (17)$$

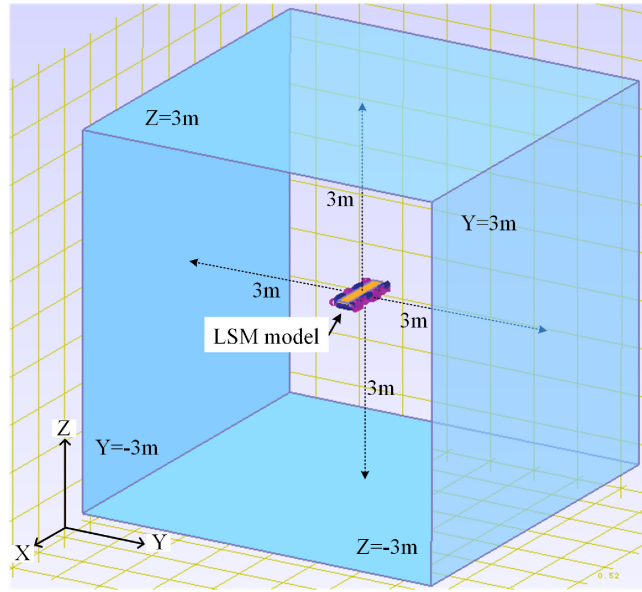


**Figure 4.** Simulation model for obtaining training data.

where SSE denotes the sum of squares due to error, while TSS denotes the total sum of squares.  $a$  denotes the quantity of sample data, and  $b$  is the quantity input variables. A value of 1 of  $R_{adj}^2$  indicates the network replicate of the surface current characteristics on stator core faultlessly. The overall adjusted R-squares of trained neural networks  $\mathbf{net}_m(\cdot)$  ( $m = 1, 2, 3$ ) are 0.9665, 0.9380 and 0.9495, respectively.

To visualize the training results, we use the proposed neural-network-based (NN-based) method to produce radiated patterns of LSM at 3-phase balanced condition on observing planes indicated in Fig. 4. Feed the trained neural network models by input data of training sets, the actual output of neural network models related to each observing point is obtained. Then, in accordance with Eq. (14), LSM radiated magnetic characteristics on each observing point could be computed. The simulated results and NN-based method results are compared in Fig. 5. The comparison indicates that there is great consistency between numerical simulation results and the radiated pattern reconstructed by NN-based model. The proposed model is capable of characterizing the overall magnetic field distribution on observing planes, and its reconstruction performance on horizontal planes is higher than that on vertical planes.

### 3.3. Validation of Method Efficiency

To further verify the efficiency of proposed NN-based model, we build a multi-source scenario to compare the time consumption difference between numerical simulation and proposed model. In the actual maglev system, LSM stator pairs are installed on both sides of maglev route at a distance of 2380 mm. The elevated maglev route is normally constructed at a relative altitude about a dozen meters to the ground plane. Therefore, as shown in Fig. 6, we build a pair of stator units with ground plane in the numerical simulation software. In both 3-phase balanced condition and short-phase fault condition, the planar radiation characteristics with an area of  $400\text{ m}^2$  at 1 m height are evaluated. The frequency and amplitude of excitation current are 300 Hz and 1800 A, and the winding with initial phase  $\varphi_1 = 0$  in left LSM model is defined as faulted phase in short-phase condition.

To solve the same case by proposed NN-based method, the ground plane is considered as a perfectly conducting surface; therefore, reflected field by ground could be obtained according to Image Theory. The field values on observing area are computed with a computation step of 1 m.

The radiation patterns of NN-based model and numerical simulation are compared in Fig. 7. In NN-based method's patterns, the range of central high amplitude area is relatively larger than that in numerical simulation patterns. However, in general, the NN-based method leads to a high degree of

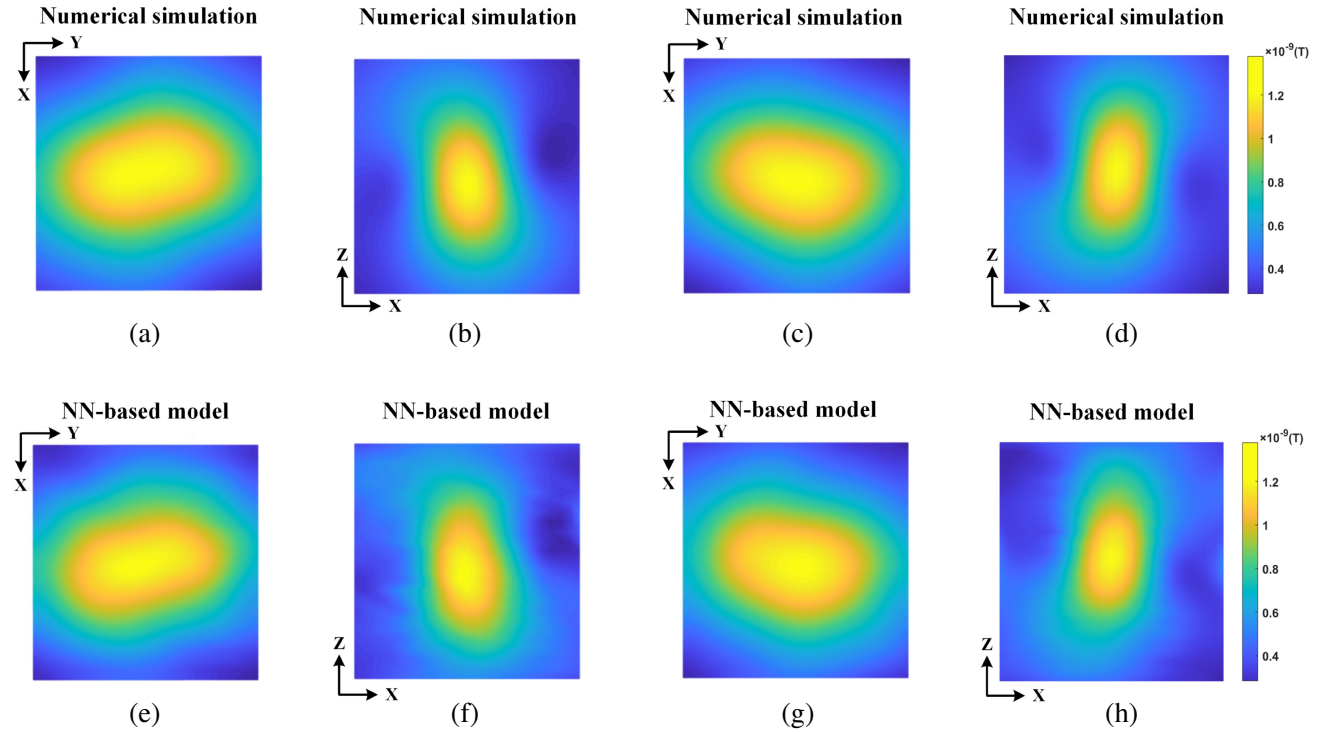


**Figure 5.** Magnetic flux density computation results of (a) numerical model and (b) NN-based equivalent model on  $Z = 3$  m plane. Magnetic flux density computation results of (c) numerical model and (d) NN-based equivalent model on  $Y = 3$  m plane. Magnetic flux density computation results of (e) numerical model and (f) NN-based equivalent model on  $Z = -3$  m plane. Magnetic flux density computation results of (g) numerical model and (h) NN-based equivalent model on  $Y = -3$  m plane.

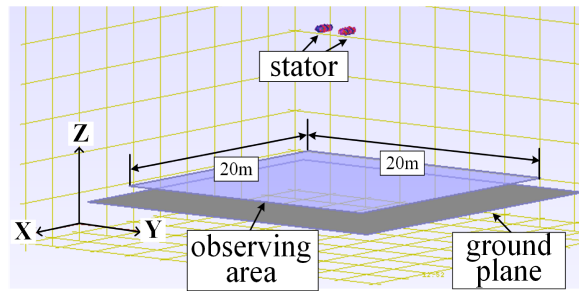


**Figure 6.** Multi-source model built in numerical simulation software.

similarity towards simulation results in the variation trend of radiation and the overall pattern. The Mean Absolute Percentage Error (MAPE) values between simulated results and computed results of NN-based method in 3-phase balanced condition and fault condition are 7.11% and 4.95%. It could be noticed that the MAPE of fault case is better than that of balanced case. As the error due to each phase of NN-based method could accumulate in the calculation, it is logical to see better accuracy in short-phase fault case.

A comparison of the computation efficiency of numerical simulation model and equivalent model using the same PC is shown in Table 1. It is obvious that the time consumption as well as energy consumption to obtain motor radiation pattern has seen a great reduction both in 3-phase balanced operating condition and short-phase fault condition. In this case, as the time consumption of numerical computation method largely depends on the size of computation region, while the time consumption

**Table 1.** Time & energy consumption comparison between numerical simulation and NN-based method.

LSM condition	Time/energy consumption of numerical simulation	Time/energy consumption of NN-based model
Balanced	18256 s/0.406 kW·h	556 s/0.012 kW·h
Short-phase fault	18401 s/0.409 kW·h	452 s/0.009 kW·h

of proposed model fully depends on the quantity of observing points, the proposed model would achieve far better computation effectiveness in evaluating the radiated pattern over long distance. The calculation using the numerical simulation requires the PC to operate at full power, and the total energy consumption is up to 0.4kW·h. In contrast, the energy consumption of the PC is controlled below 0.015 kW·h when the equivalent model is used, which greatly saves energy consumption and computing resources.

In Table 2, we compare the performance of proposed model with prior similar equivalent source models for motor radiation estimation. As the motor device in [33] is oversimplified into dipole model for high computational efficiency, it lacks ability to estimate motor radiation in various operating condition. The evaluation region of this NN-based dipole model is also restricted to one certain point. The PSO-based model proposed in [32] is capable to characterize motor radiation pattern in multi-source environment. However, as simplified wire structure is designed to reconstruct motor radiation in fixed operating mode, the PSO-based model is nonfunctional in various operating condition evaluation. By

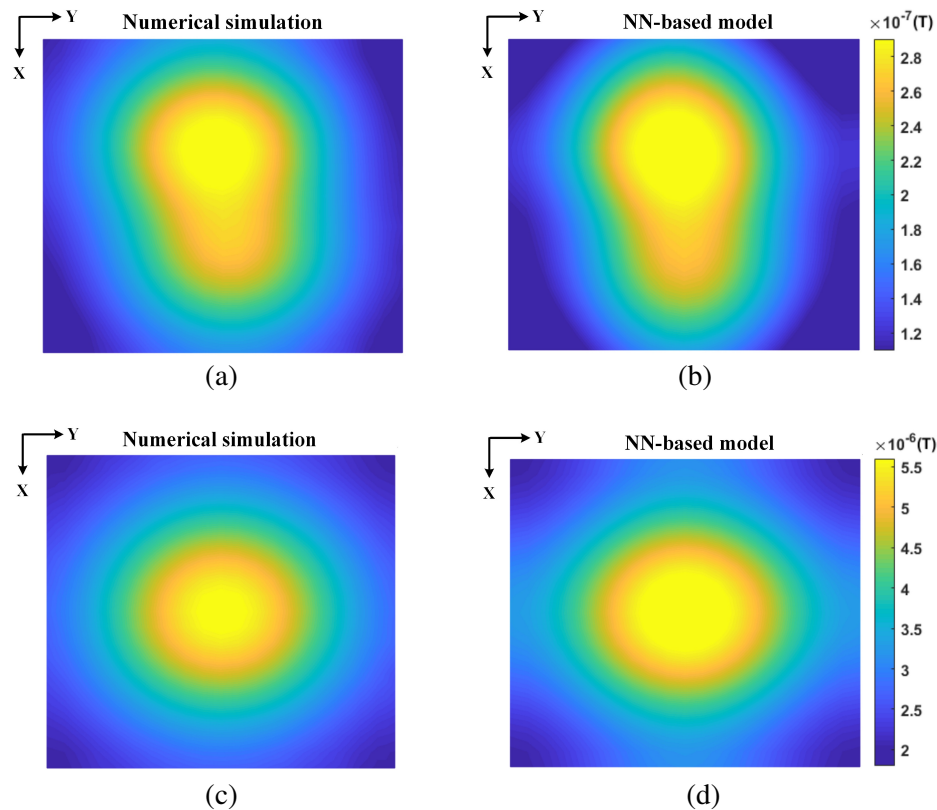


**Figure 7.** Magnetic flux density computation results of (a) numerical model and (b) NN-based equivalent model in 3-phase balanced condition. Magnetic flux density computation results of (c) numerical model and (d) NN-based equivalent model in short-phase fault condition.

**Table 2.** Performance comparison with prior motor radiation estimation method.

Performance	NN-based dipole model [33]	PSO-based wire model [32]	Proposed model
Multi-source environment evaluation	Not introduced	Capable	Capable
Various operating condition evaluation	Not introduced	Not introduced	Capable
Computational region	Only on certain point	3-D space	3-D space
Accuracy comparing with full numerical model	Satisfied (Not quantified)	Satisfied (Not quantified)	Satisfied (MAPE = 7.11% in normal condition MAPE = 4.95% in fault condition)

comparison, the proposed method moderately simplifies the LSM structure and develops separated source components, which enable proposed NN-based model to reach satisfying accuracy when being applied to multi-source radiation estimation in both normal operating condition and short-phase fault condition.

#### 4. CONCLUSION

In this paper, an equivalent source is proposed to replicate numerical simulation results and achieve a rapid estimation of LSM radiation under different operating conditions. We develop the equivalent source model following the basic concept of Source Reconstruction Method and embed neural networks in solving equivalent model's electrical parameters for a rapid computation. This neural-network-based model is proved to be effective in estimating the long-frequency magnetic field impact of LSM with a satisfying accuracy, while its time consumption is only 1/32 of the numerical simulation. In our future work, further validation of the LSM equivalent model would be processed using actual measurement data, and the proposed source reconstruction method would be expanded to equivalent source modelling of similar motor devices for rapid evaluation purpose.

#### ACKNOWLEDGMENT

This work is supported by the National Natural Science Foundation of China (Grant No. U1734203), Basic Research Business Expenses of Beijing Jiaotong University — Special Project of Frontier Science Center of Smart High Speed Railway System (Grant No. 2020JBZD004) and China Scholarship Council (Grant No. 201807090048).

#### REFERENCES

1. Liao, Z., J. Yue, and G. Lin, "Application research of hts linear motor based on halbach array in high speed maglev system," *IEEE Transactions on Applied Superconductivity*, Vol. 31, No. 5, 1–7, 2021.
2. Wang, H., J. Li, R. Qu, J. Lai, H. Huang, and H. Liu, "Study on high efficiency permanent magnet linear synchronous motor for maglev," *IEEE Transactions on Applied Superconductivity*, Vol. 28, No. 3, 1–5, 2018.
3. Glatzel, K., G. Khurdok, and D. Rogg, "The development of the magnetically suspended transportation system in the Federal Republic of Germany," *IEEE Transactions on Vehicular Technology*, Vol. 29, No. 1, 3–17, 1980.

4. Boldea, I., A. Trica, G. Papusoiu, and S. A. Nasar, "Field tests on a maglev with passive guideway linear inductor motor transportation system," *IEEE Transactions on Vehicular Technology*, Vol. 37, No. 4, 213–219, 1988.
5. Shi, X.-Y. and J.-C. Liu, "Actual measurement and evaluation of electromagnetic environment for the moving maglev train," *2020 International Conference on Microwave and Millimeter Wave Technology (ICMMT)*, 1–3, 2020.
6. Shao, J., Y. Wen, and G. Wang, "Magnetic field analysis of linear motor for high-speed maglev train," *2020 IEEE MTT-S International Conference on Numerical Electromagnetic and Multiphysics Modeling and Optimization (NEMO)*, 1–4, 2020.
7. Zhang, J., L. Xing, D. Zhang, and J. Xiao, "Modeling and simulation for electromagnetic emission of maglev train," *2019 URSI Asia-Pacific Radio Science Conference (AP-RASC)*, 2019.
8. Wang, Y. and Y. Wen, "Electromagnetic emission of maglev vehicle by linear synchronous motor," *2019 IEEE 3rd International Electrical and Energy Conference (CIEEC)*, 1507–1512, 2019.
9. Ala, G., M. C. Di Piazza, G. Tine, F. Viola, and G. Vitale, "Numerical simulation of radiated EMI in 42 V electrical automotive architectures," *IEEE Transactions on Magnetics*, Vol. 42, No. 4, 879–882, 2006.
10. Borgeest, K., "Practical papers, articles and application notes: EMC aspects of car communication systems," *IEEE Electromagnetic Compatibility Magazine*, Vol. 1, No. 1, 35–41, 2012.
11. Chiqovani, G., I. Oganezova, G. Gabriadze, M. Kuehn, M. Messer, and R. Jobava, "Radiation of low frequency magnetic field from high voltage powertrain systems of electric vehicles," *2019 International Symposium on Electromagnetic Compatibility — EMC Europe*, 968–971, 2019.
12. Li, C., J. Lin, J. Lei, T. Wu, D. Qi, and R. Chen, "Dosimetry assessment for human exposure to extremely low frequency magnetic fields in the electric vehicles," *2018 12th International Symposium on Antennas, Propagation and EM Theory (ISAPE)*, 1–4, 2018.
13. He, Y., W. Sun, P. S. W. Leung, T. Y. M. Siu, and K. T. Ng, "Impact on human exposure to low frequency radiation with psychological and brainwave changes," *2018 IEEE International Symposium on Electromagnetic Compatibility and 2018 IEEE Asia-Pacific Symposium on Electromagnetic Compatibility (EMC/APEMC)*, 936–939, 2018.
14. Karabetsos, E., E. Kalampaliki, and D. Koutounidis, "Testing hybrid technology cars: Static and extremely low-frequency magnetic field measurements," *IEEE Vehicular Technology Magazine*, Vol. 9, No. 4, 34–39, 2014.
15. Igarashi, A., K. Kobayashi, H. Matsuki, G. Endo, and A. Haga, "Evaluation of damage in dna molecules resulting from very-low-frequency magnetic fields by using bacterial mutation repairing genetic system," *IEEE Transactions on Magnetics*, Vol. 41, No. 11, 4368–4370, 2005.
16. Nishizawa, S., H.-O. Ruoss, F. M. Landstorfer, and O. Hashimoto, "Numerical study on an equivalent source model for inhomogeneous magnetic field dosimetry in the low-frequency range," *IEEE Transactions on Biomedical Engineering*, Vol. 51, No. 4, 612–616, 2004.
17. Gao, X. and D. Su, "Suppression of a certain vehicle electrical field and magnetic field radiation resonance point," *IEEE Transactions on Vehicular Technology*, Vol. 67, No. 1, 226–234, 2018.
18. Ala, G., M. C. Di Piazza, G. Tine, F. Viola, and G. Vitale, "Evaluation of radiated EMI in 42-V vehicle electrical systems by FDTD simulation," *IEEE Transactions on Vehicular Technology*, Vol. 56, No. 4, 1477–1484, 2007.
19. Xu, B., Y. Yu, X. Du, L. Xiao, and C. Wang, "On the modeling of a DC motor in electric vehicle's EMC studies," *2019 International Symposium on Antennas and Propagation (ISAP)*, 1–3, 2019.
20. Barzegaran, M. R., A. Sarikhani, and O. A. Mohammed, "An equivalent source model for the study of radiated electromagnetic fields in multi-machine electric drive systems," *2011 IEEE International Symposium on Electromagnetic Compatibility*, 442–447, 2011.
21. Zhao, H., C. Li, Z. Chen, and J. Hu, "Fast simulation of vehicular antennas for V2X communication using the sparse equivalent source model," *IEEE Internet of Things Journal*, Vol. 6, No. 4, 7038–7047, 2019.

22. Sarkar, T. K. and A. Taaghhol, "Near-field to near/far-field transformation for arbitrary near-field geometry utilizing an equivalent electric current and MoM," *IEEE Transactions on Antennas and Propagation*, Vol. 47, No. 3, 566–573, 1999.
23. Wen, J., L. Ding, Y.-L. Zhang, and X.-C. Wei, "Equivalent electromagnetic hybrid dipole based on cascade-forward neural network to predict near-field magnitude of complex environmental radiation," *IEEE Journal on Multiscale and Multiphysics Computational Techniques*, Vol. 5, 227–234, 2020.
24. Kiaee, A., R. Patton, R. R. Alavi, B. Alavikia, R. Mirzavand, and P. Mousavi, "First-order correction and equivalent source reconstruction assessment for practical multiplane magnetic near-field measurements," *IEEE Transactions on Antennas and Propagation*, Vol. 68, No. 8, 6479–6482, 2020.
25. Alvarez, Y., F. Las-Heras, and M. R. Pino, "Reconstruction of equivalent currents distribution over arbitrary three-dimensional surfaces based on integral equation algorithms," *IEEE Transactions on Antennas and Propagation*, Vol. 55, No. 12, 3460–3468, 2007.
26. Xu, Z., B. Ravelo, O. Maurice, J. Gantet, and N. Marier, "Radiated EMC Kron's model of 3-D multilayer pcb aggressed by broadband disturbance," *IEEE Transactions on Electromagnetic Compatibility*, Vol. 62, No. 2, 406–414, 2020.
27. Alavi, R. R., R. Mirzavand, A. Kiaee, R. Patton, and P. Mousavi, "Detection of the defective vias in siw circuits from single/array probe(s) data using source reconstruction method and machine learning," *IEEE Transactions on Microwave Theory and Techniques*, Vol. 67, No. 9, 3757–3770, 2019.
28. Li, P. and L. J. Jiang, "Source reconstruction method-based radiated emission characterization for PCBs," *IEEE Transactions on Electromagnetic Compatibility*, Vol. 55, No. 5, 933–940, 2013.
29. Zhang, J. and J. Fan, "Source reconstruction for IC radiated emissions based on magnitude-only near-field scanning," *IEEE Transactions on Electromagnetic Compatibility*, Vol. 59, No. 2, 557–566, 2017.
30. Barzegaran, M. R. and O. A. Mohammed, "3-D FE wire modeling and analysis of electromagnetic signatures from electric power drive components and systems," *IEEE Transactions on Magnetics*, Vol. 49, No. 5, 1937–1940, 2013.
31. Isernia, T., G. Leone, and R. Pierri, "Radiation pattern evaluation from near-field intensities on planes," *IEEE Transactions on Antennas and Propagation*, Vol. 44, No. 5, 701, 1996.
32. Sarikhani, A., M. Barzegaran, and O. A. Mohammed, "Optimum equivalent models of multi-source systems for the study of electromagnetic signatures and radiated emissions from electric drives," *IEEE Transactions on Magnetics*, Vol. 48, No. 2, 1011–1014, 2012.
33. Yu, Y., X. Du, B. Xu, C. Wang, L. Xiao, and Z. Zhang, "Equivalent motor radiation of an electric vehicle based on neural network approach," *2019 International Symposium on Antennas and Propagation (ISAP)*, 1–3, 2019.
34. Hansen, J. E., *Spherical Near-field Antenna Measurements*, P. Peregrinus on behalf of the Institution of Electrical Engineers, 1988.
35. Rengarajan, S. R. and Y. Rahmat-Samii, "The field equivalence principle: Illustration of the establishment of the non-intuitive null fields," *IEEE Antennas and Propagation Magazine*, Vol. 42, No. 4, 122–128, 2000.